

Article

Study on Texture and Grain Orientation Evolution in Cold-Rolled BCC Steel by Reaction Stress Model

Ning Zhang ¹, Li Meng ^{1,*}, Wenkang Zhang ² and Weimin Mao ³

¹ Metallurgical Technology Institute, Central Iron and Steel Research Institute, Beijing 100081, China; zhangning@cisri.com.cn

² Technology Centre of Shanxi Taigang Stainless Steel Co. Ltd., Taiyuan 030003, China; zhangwk@tisco.com.cn

³ School of Materials Science and Engineering, University of Science and Technology Beijing, Beijing 100083, China; wmmao@ustb.edu.cn

* Correspondence: mengli@cisri.com.cn or li_meng@126.com

Received: 29 June 2020; Accepted: 4 August 2020; Published: 6 August 2020



Abstract: The evolution of texture and grain orientations in a cold-rolled steel of BCC structure was simulated by a reaction stress (RS) model. The results show that cold-rolled texture could be assessed based on a RS model because the stress and strain are considered to remain consistent in the deformation process. The strain consistency is actualized by the cooperation of two plastic strains and an elastic strain. The accumulation range of each reaction stress and different activation abilities of $\{110\}\langle 111 \rangle$ and $\{112\}\langle 111 \rangle$ slip systems strongly affect the calculated deformation textures. The values of reaction stress are influenced by elastic anisotropy; however, the effects are greatly reduced because its corresponding reaction stress accumulation is limited. Typical α -fiber and γ -fiber textures are achieved when the reaction stress accumulation coefficients α_{ij} s are chosen suitably. Furthermore, the α_{ij} values that are selected based on statistically calculated textures can also be used to simulate the orientation change of multiple orientations. The existence of reaction stress is able to stabilize crystallographically symmetrical orientations under rolling deformation, in which the Schmid factors of several slip systems are identical.

Keywords: BCC structure; reaction stress (RS) model; rolling; texture; orientation

1. Introduction

Rolling technology is widely used in manufacturing metals and alloys. In general, deformation texture forms during rolling, and the resultant texture will affect the following processes and determine properties of final products [1,2]. Understanding the formation and evolution of deformation texture can provide theoretical insight for texture control, thus improving material properties [3]. Other than experimental observation, the evolution of texture and crystallographic orientation can be evaluated based on simulation, which requires a reasonable and suitable model dedicated to polycrystalline plastic deformation.

Multiple models for polycrystalline plastic deformation have been developed from the original Sachs model and Taylor model. In recent years, grain interaction (GIA) model, viscoplastic self-consistent (VPSC) model, advanced lamel (ALAMEL) models and others have been proposed. With development of these models, the simulated deformation textures have been continuously improved and nicely match experimental observation [4–10]. Regarding the stress and strain consistency during simulation, it is actualized inside grain groups by GIA and ALAMEL models, in which 8 grains and 2 grains are set as a group respectively, and different relaxation is implemented inside the groups [4–7,11]. The VPSC model considers the stress and strain continuity between every deformed grain and its surrounding matrix statistically [9–11].

Compared to the models developed based on the Taylor principle, the reaction stress (RS) model evaluates the deformation process based on the stress condition. At the beginning, only external stress is considered, and the slip system with the highest Schmid factor is activated. As soon as the active slip induces plastic strain, reaction stress by neighboring grains is taken into consideration. The reaction stress is calculated based on statistical matrix. These external and intergranular reaction stresses are combined to determine the following processes [12,13]. In simulation, the intergranular continuity of strain and stress is achieved in a natural way, and the calculation method does not have a complicated hypothesis [12–15]. RS model has been increasingly applied to metals and alloys with different crystal structures, including BCC, FCC and HCP structures. For BCC structured metals and alloys, this model has been applied to tungsten, which is elastically isotropic [12–15].

Ferritic steel with BCC structure has been widely applied in industry. For example, interstitial-free (IF) steel, low carbon steel and silicon steel are being used in automatic, architectural, and electronic fields. In general, the rolling deformation texture of BCC steel is characterized as α -fiber (rolling direction (RD) of the rolled plate//<110>) and γ -fiber (normal direction (ND) of the rolled plate//<111>). The deformation textures directly affect recrystallization behaviors and anisotropic properties of the final products [1,16–18]. Therefore, it is important to understand the evolution of deformation texture. Meanwhile, the evolution of specific deformation orientation of typical texture components needs to be studied as well. Moreover, BCC structured steel has demonstrated an elastic anisotropy, in which Young's modulus in <111> crystal direction is 6 times of that in <100> direction [19]. The elastic anisotropy and its effect on the deformation process have to be taken into consideration for simulation. Therefore, as a further theoretical study based on RS model, this study helps the development of simulation work by RS model, making it more systematically and comprehensively understood.

In this paper, a RS model is used to investigate the rolling deformation behaviors of a BCC structured steel and the simulated results are compared to the experimental results and results reported in the literature. The effects of reaction stress values and ranges in different directions, strain values, the ratio of critical resolved shear stress (CRSS) of {110}<111> slip system to CRSS of {112}<111> slip system are discussed, and the influence of elastic anisotropy is also considered. The study could help to clarify the deformation process of BCC structured steel.

2. Simulation and Experimental Methods

This study focuses on the rolling deformation behavior of BCC structured steel via both theoretical simulation and experimental characterization. RS model is used to mimic the texture evolution and orientation change of typical texture components. The RS model states that, the stress of a deformed grain undergoing in a polycrystal can be depicted as Equation (1) [12–15]:

$$[\sigma_{ij}] = \sigma_y \begin{bmatrix} 0.5 & 0 & 0 \\ 0 & 0 & 0 \\ 0 & 0 & -0.5 \end{bmatrix} + \sigma_y \begin{bmatrix} 0 & \sigma'_{12}/\sigma_y & \sigma'_{13}/\sigma_y \\ \sigma'_{21}/\sigma_y & \sigma'_{22}/\sigma_y & \sigma'_{23}/\sigma_y \\ \sigma'_{31}/\sigma_y & \sigma'_{32}/\sigma_y & 0 \end{bmatrix} \quad (1)$$

σ_y is the yield strength. The index i and $j = 1, 2, 3$, and $1, 2, 3$ represents rolling direction (RD), transverse direction (TD) and normal direction (ND), respectively. σ'_{ij} represents the reaction stress, and it can be calculated based on intergranular stress and strain balance:

$$\sigma'_{ij} = -\left(\frac{G(g) \times G(m)}{G(g) + G(m)}\right) \times \varepsilon_{ij}^p(g) \quad (2)$$

$G(g)$ and $G(m)$ correspond to the shear modulus of the deformed grain and matrix, respectively, which are dependent on the orientations of the deformed grain and matrix. $\varepsilon_{ij}^p(g)$ is the shear strain of an active slip in the deformed grain.

σ_y can be illustrated by Frank-Read theory:

$$\sigma_y = \frac{\tau_c}{\mu} = \frac{Gb}{\mu d} \quad (3)$$

G is $G(g)$, b and μ are the burgers vector and the Schmid factor corresponding to the active slip system, d is the effective dislocation distance, which decreases with the increasing strain [15]. The connection between $[\sigma_{ij}]$ and the parameters, including b , μ , d , $\varepsilon_{ij}^p(g)$ as well as crystal orientation, can be obtained, and more details can be found in the literature [12–15].

What needs to be considered is that reaction stress varies in a certain range. Therefore, the accumulation coefficient α_{ij} for reaction stress is introduced to impose the upper-limit for reaction stress σ'_{ij} , as shown in Equation (4). α_{ijs} varies in the range of 0–1, and the value imposes significant effect on the texture evolution [12,15]:

$$[\sigma_{ij}]_{lim} = \begin{bmatrix} \sigma_{11} \equiv -\sigma_{33} - \sigma'_{22} & \sigma'_{12} \leq \alpha_{12}\sigma_y/2 & \sigma'_{13} \leq \alpha_{13}\sigma_y/2 \\ \sigma'_{21} \leq \alpha_{12}\sigma_y/2 & \sigma'_{22} \leq \alpha_{22}\sigma_y/2 & \sigma'_{23} \leq \alpha_{23}\sigma_y/2 \\ \sigma'_{31} \leq \alpha_{13}\sigma_y/2 & \sigma'_{32} \leq \alpha_{23}\sigma_y/2 & \sigma_{33} \equiv -\sigma_y/2 \end{bmatrix} \quad (4)$$

As the initial orientations in this study, 1000 random orientations are chosen. The calculation step is $\Delta\varepsilon_{33} = -0.0005$. The calculated results at different strains are compared to experimental results and results reported in the literature. The effects of reaction stress accumulation coefficient α_{ij} , the activation ability of $\{110\}\langle 111 \rangle$ and $\{112\}\langle 111 \rangle$ slip systems as well as strain values ε_{33} on the deformation texture are discussed systematically. In particular, the value of α_{ij} has been proven to have significant effect on the texture evolution in BCC structured tungsten [15], and thus its effect on the calculated texture is evaluated in detail. Based on the analysis, simulation parameters are optimized and are used to discuss the orientation evolution of typical texture components in BCC steel. Surface shear stress has limited effect on texture evolution. One of the reasons is that rolling is usually performed at room temperature and thus there is no considerable shear stress by surface friction. Our earlier study on tungsten shows that small surface shear stress may lead to slight a deviation of the texture component or a decrease of texture intensity, while the major texture distribution is not affected [15]. Therefore, this study does not discuss the effect of surface shear stress.

Two types of experiments were carried out in the study. First, a forged Fe-3 wt%.Si steel was annealed at 800 °C for 2 h to obtain a microstructure with an average grain size of ~200 μm , and then a 10 mm \times 10 mm \times 10 mm sample was cut from it. After being polished at the lateral plane, the sample was compressed to 5% reduction. Afterwards, the initially polished lateral plane was measured with a Zeiss GeminiSEM500 field emission scanning electron microscope (SEM) (Zeiss, Braunschweig, Germany.) to observe the slip traces, by which the strain distribution could be evaluated. The goal is to prove that the strain consistency is due to both penetrating plastic strain and local plastic strain. This hypothesis is proposed when studying the deformation behavior of BCC structured tungsten but is not verified experimentally because of difficulty to obtain experimental data. With reliable experimental results, the distribution of penetrating and local strain is discussed. Second, a Fe-0.46 wt%.Si steel was cold rolled to different reductions. Its textures before and after rolling were measured by X-ray diffraction (XRD) (Bruker, Billerica, MA, USA) using Bruker D8 advance X-ray diffractometer. The texture evolution was compared to the simulation results so that the RS model dedicated to steels with BCC structure can be comprehensively studied and its validity will be eventually confirmed.

3. Results and Discussion

The microstructure of 5% compressed silicon steel sample and the compression direction are shown in Figure 1a. Examples of typical slip traces inside grains are given in Figure 1b, and multiple slip traces along different directions in deformed grains are highlighted and deformed grains are labeled as A, B, C and D. Each slip trace corresponds to activation of a specific slip system. At the

early stage of rolling deformation, both penetrating slip and local slip can be observed in many grains. Various local slips can be generated simultaneously in a single deformed grain, such as in grain A. The same phenomenon has been reported in [15]. The penetrating plastic strains in adjacent grains do not always coordinate with each other during the deformation, and the strain continuity is achieved via the coordination of penetrating plastic slip and local plastic slip. Elastic strain is not shown in the figure, however, its role in reducing strain inconsistency cannot be ignored, and moreover its corresponding elastic reaction stress contributes to stress continuity.

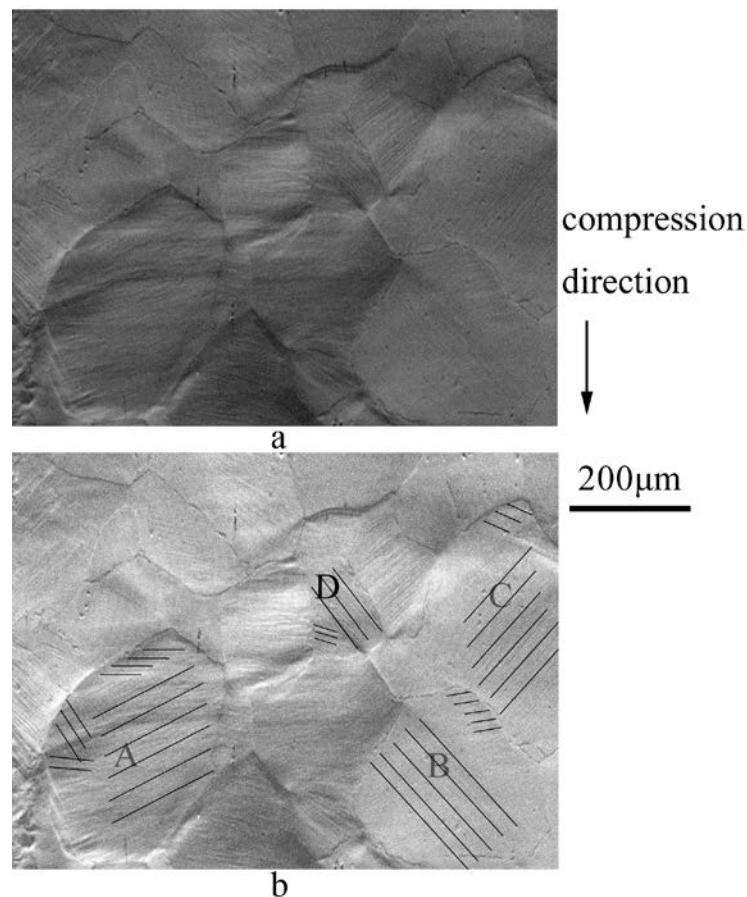


Figure 1. Lateral microstructure of silicon steel compressed to 5% reduction. (a) SEM micrograph; (b) schematic penetrating and local slip traces in some grains.

The texture evolution at different strains was calculated using various reaction stress accumulation coefficient α_{ij} , and the results when only considering $\{110\}\langle 111\rangle$ slip are shown in Figure 2(a1–d5). The effect of elastic anisotropy is not considered here. Taylor texture is obtained at low strain when α_{ijs} are set to be 0.2 in Figure 2(a1,b1), and the values of reaction stress do not exceed $0.1\sigma_y$. Under this condition, some texture components near γ -fiber, especially near $\{111\}\langle 110\rangle$ component, are weakened gradually with strain, while at the same time Taylor texture is further strengthened. When ϵ_{33} reaches -1.1 , Taylor texture becomes a major texture component and α -fiber texture starts to appear in Figure 2(c1). When the α_{ij} value increases, the calculated texture starts to deviate from α -fiber and the intensity of Taylor texture decreases. To sum up, the calculation results are similar to that of tungsten, and strong Taylor texture—which is a typical simulated rolling texture in BCC polycrystals under Taylor principle—is achieved with $\{110\}\langle 111\rangle$ slip [15].

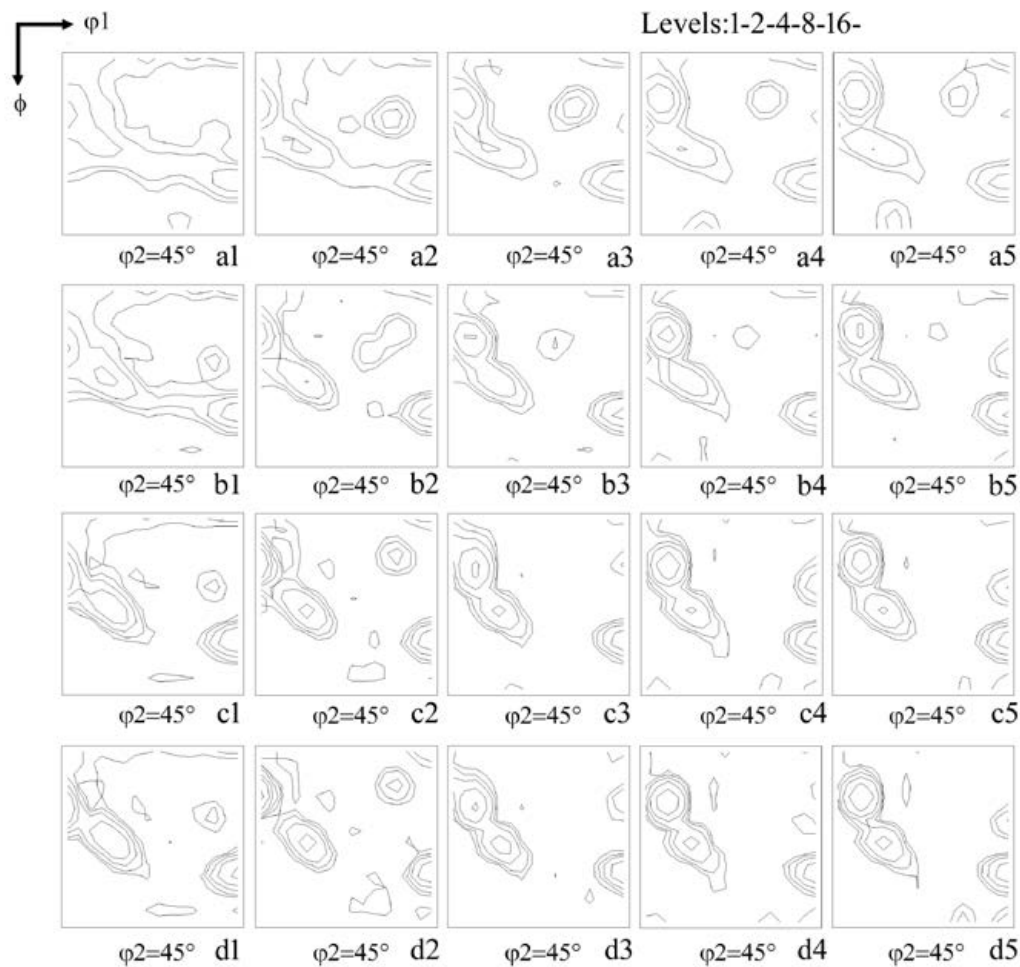


Figure 2. Calculated rolling deformation textures using reaction stress model under different ϵ_{33} and α_{ij} , $\{110\}\langle 111 \rangle$ slip. $\epsilon_{33} = -0.36$: (a1) $\alpha_{ij} = 0.2$; (a2) $\alpha_{ij} = 0.4$; (a3) $\alpha_{ij} = 0.6$; (a4) $\alpha_{ij} = 0.8$; (a5) $\alpha_{ij} = 1$; $\epsilon_{33} = -0.69$: (b1) $\alpha_{ij} = 0.2$; (b2) $\alpha_{ij} = 0.4$; (b3) $\alpha_{ij} = 0.6$; (b4) $\alpha_{ij} = 0.8$; (b5) $\alpha_{ij} = 1$; $\epsilon_{33} = -1.1$: (c1) $\alpha_{ij} = 0.2$; (c2) $\alpha_{ij} = 0.4$; (c3) $\alpha_{ij} = 0.6$; (c4) $\alpha_{ij} = 0.8$; (c5) $\alpha_{ij} = 1$; $\epsilon_{33} = -1.6$: (d1) $\alpha_{ij} = 0.2$; (d2) $\alpha_{ij} = 0.4$; (d3) $\alpha_{ij} = 0.6$; (d4) $\alpha_{ij} = 0.8$; (d5) $\alpha_{ij} = 1$.

The elastic anisotropy of Fe should be taken into consideration in the simulation because of its effect on multiple parameters, including reaction stress, slip system, orientation change and texture evolution. The textures at $\epsilon_{33} = -1.1$ are calculated with consideration of elastic anisotropy. The results are shown in Figure 3. By comparing Figure 3(a1–a5) and Figure 2(c1–c5), it is obvious that the effect of elastic anisotropy is weak when other parameters remain unchanged. The orientation dependent G_{ij} affects the value of σ'_{ij} , while it could not accumulate with no limits owing to the existence of reaction stress accumulation upper-limits. Therefore, the influence of elastic anisotropy on the calculated texture is restricted under current conditions. However, it may affect grains with certain orientations, and thus it should still be included in the simulation presented in the following sections.

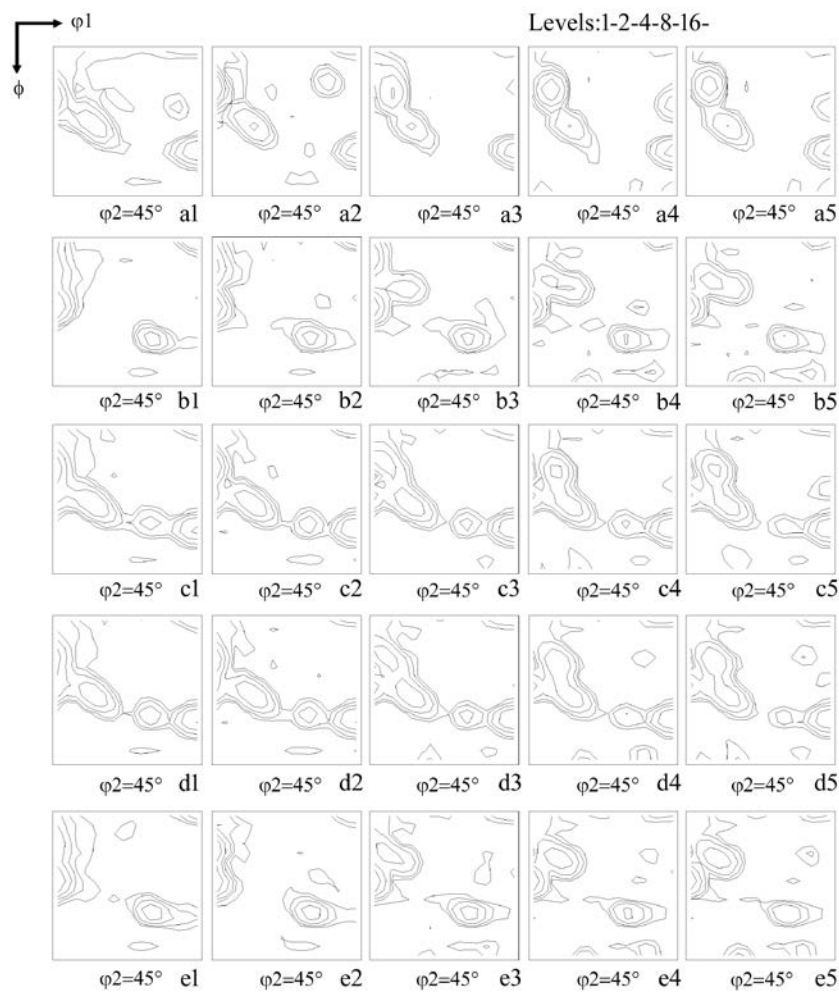


Figure 3. Effects of α_{ijs} on calculated rolling deformation textures at $\epsilon_{33} = -1.1$ when considering different activation abilities of $\{110\}\langle 111 \rangle$ and $\{112\}\langle 111 \rangle$ slip systems. $\{110\}\langle 111 \rangle$ slip: (a1) $\alpha_{ijs} = 0.2$; (a2) $\alpha_{ijs} = 0.4$; (a3) $\alpha_{ijs} = 0.6$; (a4) $\alpha_{ijs} = 0.8$; (a5) $\alpha_{ijs} = 1$; $\{112\}\langle 111 \rangle$ slip: (b1) $\alpha_{ijs} = 0.2$; (b2) $\alpha_{ijs} = 0.4$; (b3) $\alpha_{ijs} = 0.6$; (b4) $\alpha_{ijs} = 0.8$; (b5) $\alpha_{ijs} = 1$; $CRSS_{\{110\}\langle 111 \rangle} / CRSS_{\{112\}\langle 111 \rangle} = 0.95$: (c1) $\alpha_{ijs} = 0.2$; (c2) $\alpha_{ijs} = 0.4$; (c3) $\alpha_{ijs} = 0.6$; (c4) $\alpha_{ijs} = 0.8$; (c5) $\alpha_{ijs} = 1$; $CRSS_{\{110\}\langle 111 \rangle} / CRSS_{\{112\}\langle 111 \rangle} = 1$: (d1) $\alpha_{ijs} = 0.2$; (d2) $\alpha_{ijs} = 0.4$; (d3) $\alpha_{ijs} = 0.6$; (d4) $\alpha_{ijs} = 0.8$; (d5) $\alpha_{ijs} = 1$; $CRSS_{\{110\}\langle 111 \rangle} / CRSS_{\{112\}\langle 111 \rangle} = 1.05$: (e1) $\alpha_{ijs} = 0.2$; (e2) $\alpha_{ijs} = 0.4$; (e3) $\alpha_{ijs} = 0.6$; (e4) $\alpha_{ijs} = 0.8$; (e5) $\alpha_{ijs} = 1$.

The activation abilities of $\{110\}\langle 111 \rangle$ and $\{112\}\langle 111 \rangle$ slip systems are known to greatly influence the calculated texture. With different critical resolved shear stress ratios of $\{110\}\langle 111 \rangle$ vs $\{112\}\langle 111 \rangle$ slip systems ($CRSS_{\{110\}\langle 111 \rangle} / CRSS_{\{112\}\langle 111 \rangle}$), the change of calculated texture with varied α_{ijs} is also illustrated in Figure 3. Compared to the result under $\{110\}\langle 111 \rangle$ slip, $\{112\}\langle 111 \rangle$ slip promotes the formation of α -fiber texture in Figure 3(b1–b5). When α_{ijs} is low, $\{112\}\langle 111 \rangle$ slip results in higher percentage of $\{001\}\langle 110 \rangle$ texture. Stronger $\{001\}\langle 110 \rangle$ texture has been reported in silicon steel with higher Si content, and it is suggested that solute Si in the steel makes the activation of $\{112\}\langle 111 \rangle$ slip systems easier, resulting in the formation of $\{001\}\langle 110 \rangle$ texture [20]. This assumption can also be applied to the calculated result shown in Figure 3. Besides $\{001\}\langle 110 \rangle$ texture, α -fiber component between $\{112\}\langle 110 \rangle$ and $\{111\}\langle 110 \rangle$ is also present. When $CRSS_{\{110\}\langle 111 \rangle} / CRSS_{\{112\}\langle 111 \rangle} = 1.05$, the calculated texture is similar to that when only $\{112\}\langle 111 \rangle$ slip considered, as shown in Figure 3(e1–e5). The slight decrease of $\{001\}\langle 110 \rangle$ texture in Figure 3 proves the enhanced effect of $\{112\}\langle 111 \rangle$ slip on $\{001\}\langle 110 \rangle$ texture. The results in Figure 3(c1–c5, d1–d5) are due to both $\{110\}\langle 111 \rangle$ and $\{112\}\langle 111 \rangle$ slips. In other words, when $CRSS_{\{110\}\langle 111 \rangle} / CRSS_{\{112\}\langle 111 \rangle}$ values are either 0.95 or 1, alternative $\{110\}\langle 111 \rangle$ and $\{112\}\langle 111 \rangle$ slips are activated during rolling deformation. When the activation of $\{110\}\langle 111 \rangle$ slip

systems becomes easier, as shown in Figure 3(c1), the distribution of near γ -fiber texture is relatively more continuous.

According to the results in Figures 2 and 3, a set of low α_{ijs} contribute to formation of typical α -fiber and γ -fiber textures in BCC steel but also cause the γ -fiber texture to deviate to Taylor component. Taylor texture is obtained due to reaction stress, and thus it is assumed that lower α_{ijs} may lead to more exact γ -fiber texture. The effect of α_{13} and α_{23} on the deformation texture is shown in Figure 4 when α_{12} and α_{22} are set as 0.2 and as 0 or 0.1, respectively. α_{ijs} are selected based on the methods reported in our previous works [12–15]. In general, compared to ε_{12} , ε_{13} and ε_{23} tend to occur easier and show distinct characteristic under rolling deformation [12,21]. The value of $\text{CRSS}_{\{110\}\langle 111\rangle}/\text{CRSS}_{\{112\}\langle 111\rangle}$ is chosen to be 0.95, suggesting that $\{110\}\langle 111\rangle$ slip is presumed to be more likely to be activated [20]. As shown in Figure 4, when α_{13} and α_{23} vary between 0 and 0.08, the calculated texture is a mixture of α -fiber and γ -fiber textures [2,22–24]. Therefore, it can be deduced that for BCC steel, the maximum accumulation of σ'_{12} is about $0.1\sigma_y$, and the existence of σ'_{12} is critical for obtaining γ -fiber texture. In comparison, the accumulation of σ'_{13} and σ'_{23} is restricted in a smaller range. Comparing Figure 4A(a1–c3) to Figure 4B(a1–c3), the $\{111\}\langle 110\rangle$ texture is attributed to σ'_{22} , while the value of α_{22} still needs to remain small to prevent forming uneven γ -fiber. When α_{13} and α_{23} are discussed in a small range, respectively, their effects on texture evolution interacts with each other and shows a relationship with α_{22} . In detail, at the same α_{23} , higher α_{13} increases α -fiber texture, while different α -fiber texture components occur due to varied α_{22} , and $\{111\}\langle 110\rangle$ texture is achieved when α_{22} is 0.1. At the same α_{13} , higher α_{23} promotes $\{111\}\langle 112\rangle$ texture, however, the $\{111\}\langle 112\rangle$ texture deviates towards Taylor texture when α_{13} increases to 0.08. It concludes that the calculation process is similar to that when tungsten is used, whereas the specific α_{ij} values corresponding to the reasonable simulated textures are different [15].

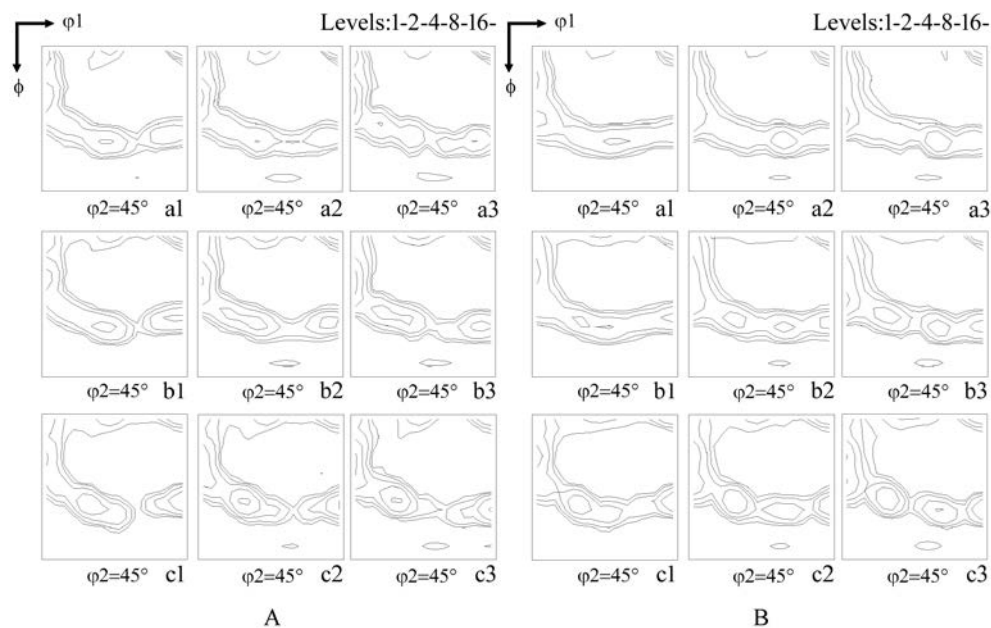


Figure 4. The effect of α_{13} , α_{23} and α_{22} not higher than 0.08 on calculated texture when using $\alpha_{12} = 0.2$ and $\text{CRSS}_{\{110\}\langle 111\rangle}/\text{CRSS}_{\{112\}\langle 111\rangle} = 0.95$. (A) $\alpha_{22} = 0$: (a1) $\alpha_{13} = \alpha_{23} = 0$; (a2) $\alpha_{13} = 0.04$, $\alpha_{23} = 0$; (a3) $\alpha_{13} = 0.08$, $\alpha_{23} = 0$; (b1) $\alpha_{13} = 0$, $\alpha_{23} = 0.04$; (b2) $\alpha_{13} = \alpha_{23} = 0.04$; (b3) $\alpha_{13} = 0.08$, $\alpha_{23} = 0.04$; (c1) $\alpha_{13} = 0$, $\alpha_{23} = 0.08$; (c2) $\alpha_{13} = 0.04$, $\alpha_{23} = 0.08$; (c3) $\alpha_{13} = \alpha_{23} = 0.08$. (B) $\alpha_{22} = 0.1$: (a1) $\alpha_{13} = \alpha_{23} = 0$; (a2) $\alpha_{13} = 0.04$, $\alpha_{23} = 0$; (a3) $\alpha_{13} = 0.08$, $\alpha_{23} = 0$; (b1) $\alpha_{13} = 0$, $\alpha_{23} = 0.04$; (b2) $\alpha_{13} = \alpha_{23} = 0.04$; (b3) $\alpha_{13} = 0.08$, $\alpha_{23} = 0.04$; (c1) $\alpha_{13} = 0$, $\alpha_{23} = 0.08$; (c2) $\alpha_{13} = 0.04$, $\alpha_{23} = 0.08$; (c3) $\alpha_{13} = \alpha_{23} = 0.08$.

Based on previous results and discussion, the simulation process and selected parameters can be further optimized so that the calculated textures match more closely to the real deformation process [2,23,24]. As shown in Figure 5, typical α -fiber and γ -fiber textures are obtained at 50%

reduction, and both textures are enhanced with increasing strain. $\{111\}\langle 110\rangle$ texture as well as other α -fiber texture components becomes stronger while $\{111\}\langle 112\rangle$ texture is weakened at higher strain. When the accumulation of σ'_{23} is permitted, compared to the situation of relaxing σ'_{23} in Figure 5(a1–a3), stronger $\{111\}\langle 112\rangle$ texture is shown in Figure 5(c1–c3). When comparing Figure 5(a1–a3) and Figure 5(b1–b3), the preferred $\{110\}\langle 111\rangle$ slip leads to stronger $\{112\}\langle 110\rangle$ texture than $\{001\}\langle 110\rangle$ texture. The stronger $\{111\}\langle 110\rangle$ texture is also observed at higher strain.

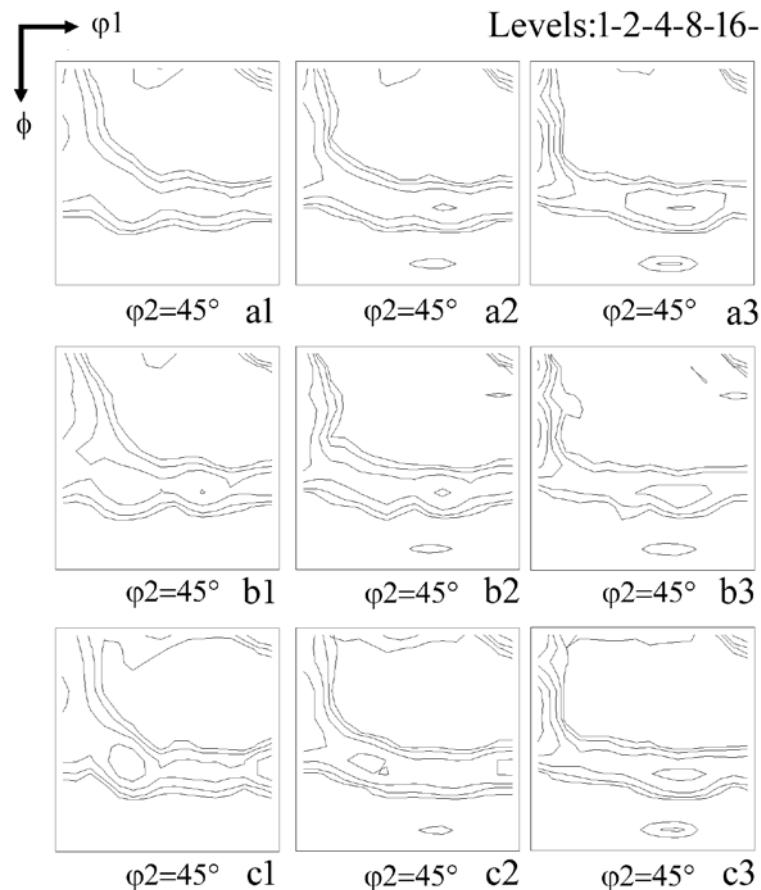


Figure 5. The calculated rolling deformation textures under different strains when using $\alpha_{12} = 0.2$, $\alpha_{13} = 0.04$, $\alpha_{22} = 0.04$ while different α_{23} and $\text{CRSS}_{\{110\}\langle 111\rangle}/\text{CRSS}_{\{112\}\langle 111\rangle}$ values. $\alpha_{23} = 0$, $\text{CRSS}_{\{110\}\langle 111\rangle}/\text{CRSS}_{\{112\}\langle 111\rangle} = 0.95$: (a1) $\epsilon_{33} = -0.69$, (a2) $\epsilon_{33} = -1.1$, (a3) $\epsilon_{33} = -1.6$; $\alpha_{23} = 0$, $\text{CRSS}_{\{110\}\langle 111\rangle}/\text{CRSS}_{\{112\}\langle 111\rangle} = 1$: (b1) $\epsilon_{33} = -0.69$, (b2) $\epsilon_{33} = -1.1$, (b3) $\epsilon_{33} = -1.6$; $\alpha_{23} = 0.04$, $\text{CRSS}_{\{110\}\langle 111\rangle}/\text{CRSS}_{\{112\}\langle 111\rangle} = 0.95$: (c1) $\epsilon_{33} = -0.69$, (c2) $\epsilon_{33} = -1.1$, (c3) $\epsilon_{33} = -1.6$.

Since the simulated textures in Figure 5 show characteristics of a typical rolling deformation texture of BCC structured steel, the selection of corresponding calculation parameters is proved to be reasonable. The experimental measurement shown in Figure 6 illustrates the texture evolution of a cold rolled Fe-Si steel. A weak texture with an intensity less than 1.4 is displayed in the sample prior to rolling, which is similar to that used in the simulation. The cold-rolling process generated α -fiber and γ -fiber textures in 52% ($\epsilon_{33} = -0.73$) steel, as shown in Figure 6b. When the rolling reduction increases to 80% ($\epsilon_{33} = -1.6$), the peak of γ -fiber changes from $\{111\}\langle 112\rangle$ to $\{111\}\langle 110\rangle$ in Figure 6c. At the same time, α -fiber texture is also enhanced. The texture demonstrates a similar evolution process as the simulated results in Figure 5. Therefore, RS model is considered to be applicable for texture simulation for BCC steel, and the parameters in Figure 5 can be used for simulating this rolling process. Confirmed by both theoretical and experimental analysis, for this Si-Fe material, the $\{110\}\langle 111\rangle$ slip system is easier to be activated to achieve a strong $\{112\}\langle 110\rangle$ texture at high strain, and the accumulation of ϵ_{23} should be permitted while in lower range than Figure 5(c1–c3).

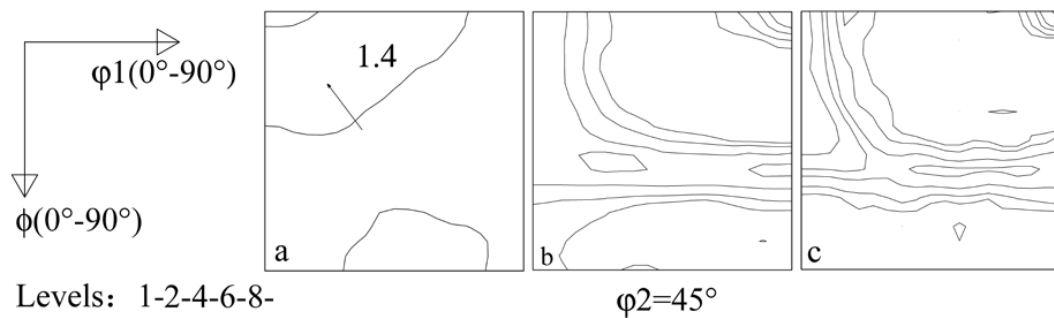


Figure 6. Measured textures of a Fe-0.46wt%Si steel. (a) Prior to rolling; (b) 52% reduction; (c) 80% reduction.

To sum up, when calculating the texture evolution in BCC steel, the applied assumptions include a moderate accumulation of σ'_{12} and much narrower range of the rest of σ'_{ijs} . Similar to relaxed constraint (RC) model, the strain consistency of ε_{13} and ε_{23} is easy to be fulfilled or be compensated by local slip. Through this compensation strategy, the strain continuity in some directions is relaxed and the simulated result is more reasonable than that by Taylor model [25,26]. Although modification of simulation parameters will cause minor changes in the simulated results, major texture distribution and evolution trend remains stable.

It is worth noting that RS model considers the deformation process in a statistical view and the orientation change of major grains contributes to the statistical texture evolution. RS model can also be used to analyze the orientation evolution of many texture components. Based on previous discussions, the calculation parameters used in Figure 5(a1–a3) are selected for theoretically analyzing the evolutions of {001}, {110}, α -fiber and γ -fiber orientations under rolling deformation. These orientations are commonly observed in BCC steels: {001} orientation corresponds to columnar grains; {110} orientations including Goss and brass components are usually obtained after hot rolling silicon steel; α -fiber and γ -fiber texture can be achieved after both hot and cold rolling.

In Figure 7(a1,a3), {001}<100>((45° 0° 45°)) and {001}<110>((0° 0° 45°)) orientations are stable under rolling deformation, and no changes in orientation are observed. Cube orientation shows meta-stability during rolling in silicon steel [27], and stable end {001}<110> orientation is widely reported [28,29]. {001}<120>((20° 0° 45°)) orientation tends to rotate towards α -fiber and deviate from {001}-fiber simultaneously in Figure 7(a2). A similar crystal rotation route is observed in other researchers' work [27,30] as well as in our previous report when investigating the occurrence of {001}<112>-{113}<361> texture in silicon steel. Stability in {112}<110>((0° 35° 45°)) orientation is also confirmed, and the α -fiber components between it and {001}<110> components rotate to them alternatively in Figure 7(b1–b3), depending on which component it is initially closer to. In consequence, {001}<110> and {112}<110> textures on α -fiber become stronger with strain, as shown in Figure 5. As far as the γ -fiber components are concerned, as shown in Figure 7(c1–c3), {111}<110>((0° 55° 45°)) orientation rotates towards {112}<110> orientation, whereas {111}<112>((30° 55° 45°)) orientations show strong stability and barely shift to other orientations. The (15° 55° 45°) orientation firstly rotates to {111}<110> orientation and then transits to {112}<110> orientation. Therefore, it can be deduced that strengthening {111}<110> texture with increasing strain may be not only due to its stability, but also affected by rotation from other orientations. For {110} shear texture components in Figure 7(d1–d3), Goss((90° 90° 45°)) orientation is stable at the early stage but rotates to {111}<112> orientation at higher strain; {110}<229>((75° 90° 45°)) orientation rotates to γ -fiber closer to {111}<112> orientation in the beginning of rolling and then turns to near {111}<110> orientation; brass orientation((60° 90° 45°)) shows a transition route from γ -fiber towards α -fiber in the end. These transition routes for {110} orientations are consistent with the experimental data reported in our early work [31]. Overall, for most of the typical orientations in Figure 7(a1–d3), the rotation preferentially revolving towards α -fiber or γ -fiber is predicted.

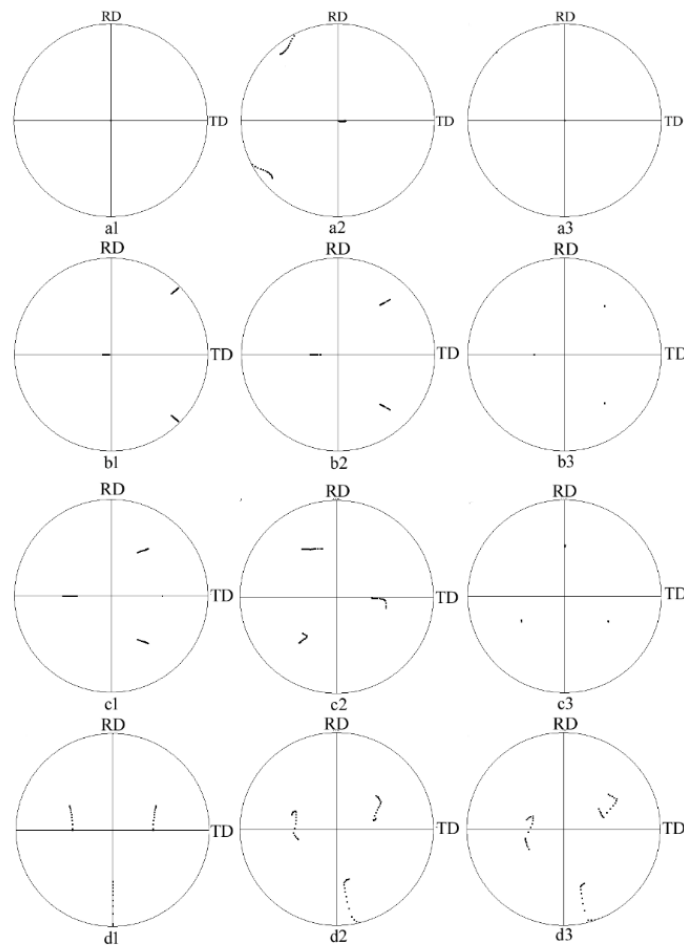


Figure 7. Calculated orientation change of typical texture components of BCC steel during rolling deformation to $\varepsilon_{33} = -1.1$, $\{200\}$ pole figures. **(a1)** ($45^\circ 0^\circ 45^\circ$); **(a2)** ($20^\circ 0^\circ 45^\circ$); **(a3)** ($0^\circ 0^\circ 45^\circ$); **(b1)** ($0^\circ 10^\circ 45^\circ$); **(b2)** ($0^\circ 20^\circ 45^\circ$); **(b3)** ($0^\circ 35^\circ 45^\circ$); **(c1)** ($0^\circ 55^\circ 45^\circ$); **(c2)** ($15^\circ 55^\circ 45^\circ$); **(c3)** ($90^\circ 55^\circ 45^\circ$); **(d1)** ($90^\circ 90^\circ 45^\circ$); **(d2)** ($75^\circ 90^\circ 45^\circ$); **(d3)** ($60^\circ 90^\circ 45^\circ$).

4. Discussion

The influence of the reaction stress accumulation coefficients α_{ijs} on the stress tensor is evident by restricting the changing range of reaction stress. When the value of reaction stress σ'_{ij} exceeds the upper-limit, it is set to be equal to the upper-limit value. According to the calculation results and discussion in this paper, the reaction stress should not be accumulated to a high level, however, moderate or even minor upper-limits are allowed. During the calculation, small reaction stress in the whole stress tensor may cause occurrence of a new slip, thus the accumulation of pre-existing reaction stress can be eliminated. Meanwhile, change in reaction stress value also affects the stress condition of neighboring grains, and the plastic slip of neighboring grains can also terminate accumulation of reaction stress. Under the combined effect of external and reaction stress with reasonable upper-limits, multiple slips are generated, and the simulated evolution tends to closely match the real situation when the calculation step is sufficiently refined.

On the other hand, moderate or even smaller α_{ij} values are the intrinsic requirement of RS model. For doing so the strain that corresponds to the elastic reaction stress will remain as elastic strain during the process. As shown in Figure 1, besides penetrating the plastic slip and elastic slip, the intergranular strain consistency requires the participation of a local plastic slip. In the case that reaction stress is restricted to the upper-limits, considering the low α_{ij} values, the corresponding elastic strain may be

much lower than the strain value used in Equation (2), thus the effect of local slip on strain consistency cannot be ignored.

During the deformation, an active slip usually causes crystal orientation to change, and the strain is accumulated if no other slip systems are activated. For polycrystals, the strain caused by active slip leads to discontinuity between a deformed grain and its environment, and this discontinuity shall be reduced by spontaneous reaction stress [15]. In this study, some crystal symmetrical orientations show stability to a certain extent under rolling deformation. Figure 7 illustrates that, $\{001\}\langle 100\rangle$ and $\{110\}\langle 001\rangle$ orientations are stable at the early rolling stage. For these symmetrical orientations, the Schmid factors of two or more slip systems are identical under external stress. For example, after a slip occurs in a grain, cube oriented single crystal shows one-directional crystal rotation around $\langle 001\rangle$ axis [28,32], and then an opposite slip system with the highest Schmid factor will be activated by the accumulated reaction stress in polycrystals. The alternative activation of two slip systems leads to the orientation stability. Meanwhile the strains caused by alternative slips are compensated by each other, and so the total strain is reduced.

5. Summary

A simulation for cold rolling deformation texture in a BCC steel is well established based on a RS model. The model considers stress and strain consistency in a natural way, in which the strain consistency is achieved by cooperation of two plastic strains and an elastic strain. The reaction stress poses significant effect on texture evolution, and varied accumulation upper-limits in different directions are indicated. With different values of reaction stress accumulation coefficient α_{ijs} , $\{110\}\langle 111\rangle$ slip leads to Taylor or γ -fiber texture, and $\{112\}\langle 111\rangle$ slip strengthens α -fiber texture, including $\{001\}\langle 110\rangle$ texture component. The elastic anisotropy influences the values of reaction stress, while the upper-limit of reaction stress noticeably reduces the effect of elastic anisotropy. As the α_{12} is set to be 0.2, typical α -fiber and γ -fiber texture are achieved even when low values of other α_{ijs} are applied in simulation. The accumulation of σ'_{12} is not high, however, its effect on texture formation is not trivial. In the meantime, the change of other reaction stress σ'_{ijs} affects the distribution of γ -fiber texture. The selected α_{ij} values based on calculated texture results can also be used to simulate the orientation change of many specific orientations, and reaction stress is shown to help crystallographically symmetrical orientations, of which the Schmid factors of several slip systems are identical, remaining stable under rolling deformation.

Author Contributions: Conceptualization, N.Z. and L.M.; software, N.Z.; formal analysis, N.Z.; investigation, N.Z.; resources, L.M. and W.Z.; data curation, N.Z.; writing—original draft preparation, N.Z.; writing—review and editing, L.M.; funding acquisition, L.M., W.Z. and W.M. All authors have read and agreed to the published version of the manuscript.

Funding: This research was funded by the National Key Research and Development Program of China (grant number 2017YFB0903901), the National Natural Science Foundation of China (grant number 51571024) and the Shanxi Provincial Science and Technology Major Special Project (grant number 20191102004). And the APC was funded by the National Key Research and Development Program of China (grant number 2017YFB0903901).

Acknowledgments: Thank you to Sheng Zhong for his English editing help.

Conflicts of Interest: The authors declare no conflict of interest.

References

1. Park, J.T.; Szpunar, J.A. Evolution of recrystallization texture in nonoriented electrical steels. *Acta Mater.* **2003**, *51*, 3037–3051. [[CrossRef](#)]
2. Kestens, L.A.I.; Pirgazi, H. Texture Formation in Metal Alloys with Cubic Crystal Structures. *Mater. Sci. Technol.* **2016**, *32*, 1303–1315. [[CrossRef](#)]
3. Das, A.J. Calculation of crystallographic texture of BCC steels during cold rolling. *Mater. Eng. Perform.* **2017**, *26*, 2708–2720. [[CrossRef](#)]

4. Engler, O.; Crumbach, M.; Li, S. Alloy-dependent rolling texture simulation of aluminium alloys with a grain-interaction (GIA) model. *Acta Mater.* **2005**, *53*, 2241–2257. [[CrossRef](#)]
5. Mu, S.J.; Tang, F.; Gottstein, G. A cluster-type grain interaction deformation texture model accounting for twinning-induced texture and strain-hardening evolution: Application to magnesium alloys. *Acta Mater.* **2014**, *68*, 310–324. [[CrossRef](#)]
6. Van Houtte, P.S.; Li, M.; Seefeldt, M.; Delannay, L. Deformation texture prediction: From the Taylor model to the advanced Lamel model. *Int. J. Plast.* **2005**, *21*, 589–624. [[CrossRef](#)]
7. Molinari, A.; Canova, G.R.; Ahzi, S. A self consistent approach of the large deformation polycrystal viscoplasticity. *Acta Metall.* **1987**, *35*, 2983–2994. [[CrossRef](#)]
8. Lebensohn, R.A.; Tomé, C.N. A self-consistent anisotropic approach for the simulation of plastic deformation and texture development of polycrystals-Application to zirconium alloys. *Acta Metall. Mater.* **1993**, *41*, 2611–2624. [[CrossRef](#)]
9. Lebensohn, R.A.; Tomé, C.A.; Castañeda, P.P. Self-consistent modelling of the mechanical behaviour of viscoplastic polycrystals incorporating intragranular field fluctuations. *Philos. Mag.* **2007**, *87*, 4287–4322. [[CrossRef](#)]
10. Lebensohn, R.A.; Turner, P.A.; Signorelli, J.W.; Canova, G.R.; Tomé, C.A. Calculation of intergranular stresses based on a large strain visco-plastic self-consistent model. *Mod. Sim. Mats. Sc. Eng.* **1998**, *6*, 447–465. [[CrossRef](#)]
11. Xie, Q.G.; Van Bael, A.; Sidor, J.; Moerman, J.; Van Houtte, P. A new cluster-type model for the simulation of textures of polycrystalline metals. *Acta Mater.* **2014**, *69*, 175–186. [[CrossRef](#)]
12. Mao, W.M. Intergranular mechanical equilibrium during rolling deformation of polycrystalline metals based on Taylor principles. *Mater. Sci. Eng. A* **2016**, *672*, 129–134. [[CrossRef](#)]
13. Mao, W.M.; Yu, Y.N. Effect of elastic reaction stress on plastic behaviors of grains in polycrystalline aggregate during tensile deformation. *Mater. Sci. Eng. A* **2004**, *367*, 277–281. [[CrossRef](#)]
14. Mao, W.M. Influence of Intergranular Mechanical Interactions on Orientation Stabilities during Rolling of Pure Aluminum. *Front. Mater. Sci.* **2018**, *12*, 322–326. [[CrossRef](#)]
15. Zhang, N.; Mao, W.M. Study on the cold rolling deformation behavior of polycrystalline tungsten. *Int. J. Refract. Met. Hard Mater.* **2019**, *80*, 210–215. [[CrossRef](#)]
16. Ray, R.K.; Jonas, J.J.; Hook, R.K. Cold rolling and annealing textures in low carbon and extra low carbon steels. *Int. Mater. Rev.* **1994**, *39*, 129–172. [[CrossRef](#)]
17. Guo, Y.H.; Wang, Z.D.; Li, S.W.; Zou, W.W. Comparison of texture and properties of IF steel with ELC Steel. *J. Northeast. Univ. (Nat. Sci.)* **2007**, *28*, 1713–1716.
18. Shen, Y.F.; Xue, W.Y.; Guo, Y.H. Effect of cold rolling and annealing on texture evolution and mechanical properties of IF steel sheet. *Steel Res. Int.* **2010**, *81*, 146–149.
19. Sung, J.K.; Lee, D.N.; Wang, D.H.; Koo, Y.M. Efficient generation of cube-on-face crystallographic Texture in iron and its alloys. *ISIJ Int.* **2011**, *51*, 284–290. [[CrossRef](#)]
20. Mao, W.M.; Yang, P. *Material Science Principles on Electrical Steels*; Higher Education Press: Beijing, China, 2013; pp. 156–157.
21. Hirsch, J.; Lücke, K. Mechanism of deformation and development of rolling texture in polycrystalline Fcc metals-II. *Acta Metall.* **1988**, *36*, 2883–2904. [[CrossRef](#)]
22. Raabe, D.; Lücke, K. Rolling and annealing textures of BCC metals. *Mater. Sci. Forum* **1994**, *157*, 597–610. [[CrossRef](#)]
23. Kestens, L.A.I.; Jacobs, S. Texture control during the manufacturing of nonoriented electrical steels. *Text. Stress Microstruct.* **2008**, *2008*, 173083. [[CrossRef](#)] [[PubMed](#)]
24. Bate, P.S.; da Fonseca, J.Q. Texture development in the cold rolling of IF steel. *Mater. Sci. Eng. A* **2004**, *380*, 365–377. [[CrossRef](#)]
25. Van Houtte, P. A comprehensive mathematical formulation of an extended Taylor-Bishop-Hill model featuring relaxed constraints, the Renouard-Wintenberger theory and a strain rate sensitivity model. *Text. Microstruct.* **1988**, *8*, 313–350. [[CrossRef](#)]
26. Leffers, T.; Jensen, D.J. Evaluation of the effect of initial texture on the development of deformation texture. *Text. Microstruct.* **1986**, *16*, 231–254. [[CrossRef](#)]
27. Sha, Y.H.; Sun, C.; Zhang, F. Strong cube recrystallization texture in silicon steel by twin-roll casting process. *Acta Mater.* **2014**, *76*, 106–117. [[CrossRef](#)]

28. Walter, J.L.; Hibbard, W.R. Texture of cold-rolled and recrystallized crystal of Silicon-Iron. *Trans. Metall. Soc. AIME* **1958**, *212*, 731–737.
29. Tsuji, N.; Tsuzaki, K.; Maki, T. Effect of initial orientation on the cold rolling behavior of solidified columnar crystals in a 19% Cr ferritic stainless steel. *ISIJ Int.* **1992**, *32*, 1319–1328. [[CrossRef](#)]
30. Zhang, N.; Yang, P.; Mao, W.M. {001}<120>-{113} <361> recrystallization textures induced by initial {001} grains and related microstructure evolution in heavily rolled electrical steel. *Mater. Character.* **2016**, *119*, 225–232. [[CrossRef](#)]
31. Zhang, N.; He, C.X.; Yang, P. Effect of {110}<229> and {110}<112> grains on texture evolution during cold rolling and annealing of electrical steel. *ISIJ Int.* **2016**, *56*, 1462–1469. [[CrossRef](#)]
32. Abe, H.; Matsuo, M.; Ito, K. Cold rolling and recrystallization textures of Silicon-Iron crystals rolled in (100)[001] orientation. *Trans. JIM* **1963**, *4*, 28–32. [[CrossRef](#)]



© 2020 by the authors. Licensee MDPI, Basel, Switzerland. This article is an open access article distributed under the terms and conditions of the Creative Commons Attribution (CC BY) license (<http://creativecommons.org/licenses/by/4.0/>).